Supporting Information for

Decoding in-plane orientation of self-assembled structures in cellulose nanopapers hybridized with tailored polymeric nanoparticles

Åsa Jerlhagen[1,2], Korneliya Gordeyeva[1,2], Martina Cattaruzza[1], Louise Brandt[1,3], Benedikt Sochor[4], Sarathlal Koyiloth Vayalil[4,5], Stephan V. Roth[1,3,4], Lars Wågberg[1,2,3], Eva Malmström[1,2,3]

[1]KTH Royal Institute of Technology, Department of Fiber and Polymer Technology, School of Engineering Sciences in Chemistry, Biotechnology and Health, Teknikringen 56, SE-100 44 Stockholm, Sweden
[2]FibRe – Centre for Lignocellulose-based Thermoplastics, KTH Royal Institute of Technology, Department of Fiber and Polymer Technology, School of Engineering Sciences in Chemistry, Biotechnology and Health, Teknikringen 56, SE-100 44 Stockholm, Sweden
[3]Wallenberg Wood Science Center, Department of Fibre and Polymer Technology, KTH Royal Institute of Technology, Teknikringen 56-58, SE-100 44 Stockholm, Sweden
[4]Deutsches Elektronen-Synchrotron DESY, Notkestrasse 85, 22607 Hamburg, Germany
[5]Advanced Light Source, Lawrence Berkeley National Laboratory, 6 Cyclotron Rd, CA 94720, Berkeley
[6]Applied Science Cluster, University of Petroleum and Energy Studies UPES, 248007 Dehradun, India
*Correspondence to: mavem@kth.se

Table of Contents

Supporting Information

1. Cellulose nanofibrils (CNFs)

Table S1. Characterization of cellulose nanofibrils (CNFs). Surface charge characterized by polyelectrolyte titration, sizes by atomic force microscopy.

Surface charge (µmol/g)	Diameter AFM (nm)	Length AFM (nm)
450 ± 20	2.56 ± 0.51	491 ± 254

2. Polymeric nanoparticles by polymerization-induced self-assembly (PISA)

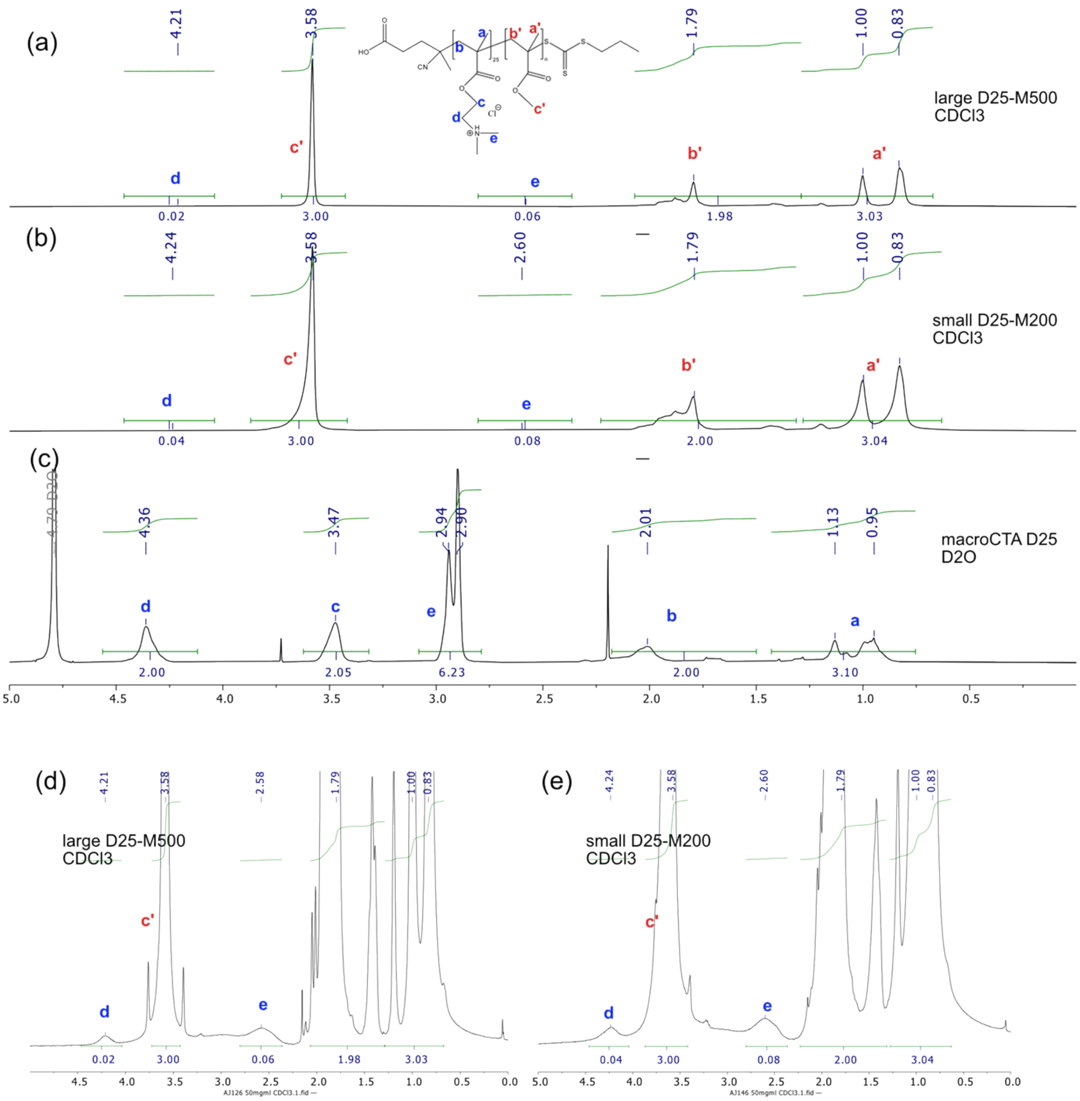

Figure S1. ^{1}H-NMR of (a) PDMAEMA macro-initiator and (b,c) PISA nanoparticle block copolymers. In the block copolymer spectra, we can see the signal from the cationic PDMAEMA segment (d,e).

However, because of the amphiphilic nature of the block copolymer, perfect solubility is not achieved in any readily available deuterated solvent. Because of the poor solubility of the DMAEMA segment in deuterated chloroform, these ^{1}H-NMR integrals underestimate the ratio between DMAEMA and MMA units.

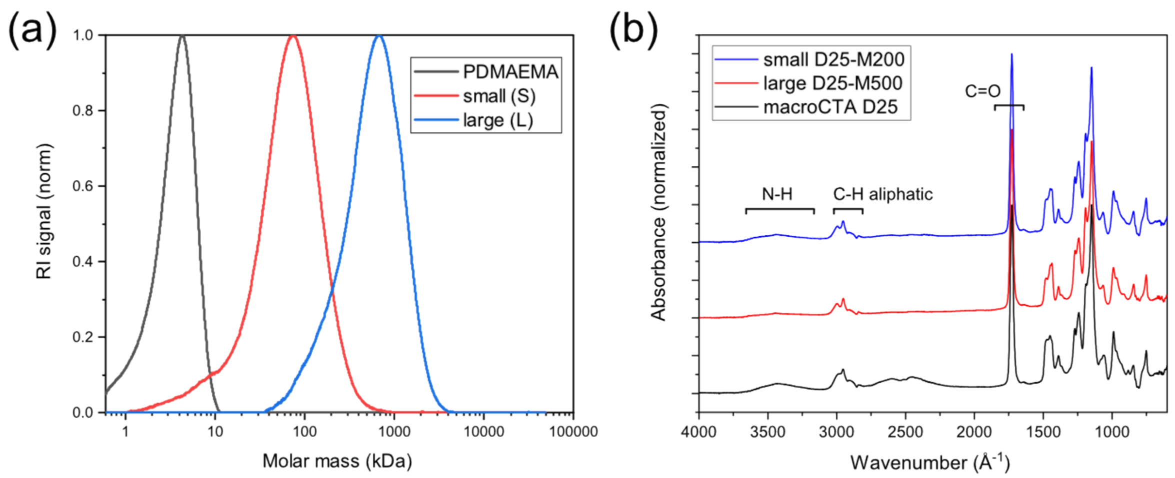

Figure S2. Characterization of PDMAEMA macro-initiator and PISA nanoparticles after chain extension with MMA. Size exclusion chromatography (SEC) in (a) shows the growth of PDMAEMA by addition of hydrophobic monomer MMA, confirming livingness. FTIR (b) shows the tertiary amine group of PDMAEMA, aliphatic C-H stretch signals and sharp carbonyl (C=O) signal of the methacrylate. This confirms that no alkene, ie unreacted monomer, is present.

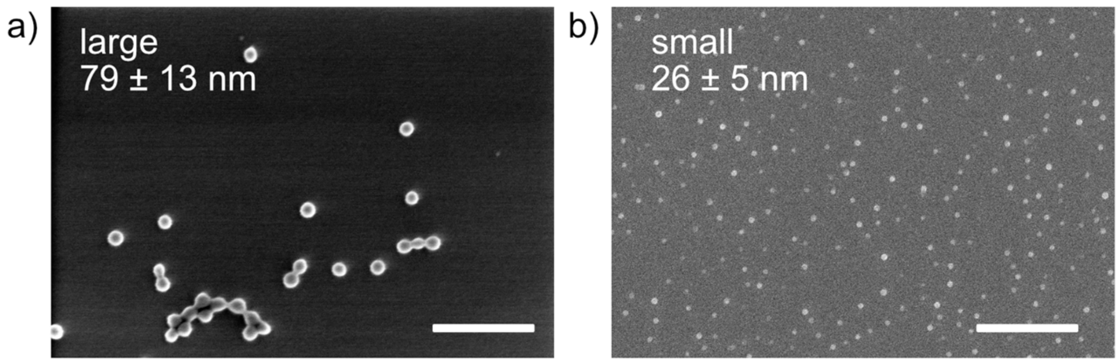

Figure S3. FE-SEM images of large (L) and small (S) polymeric nanoparticles, adsorbed to silicon wafer as substrate. Scale bar 500 nm.

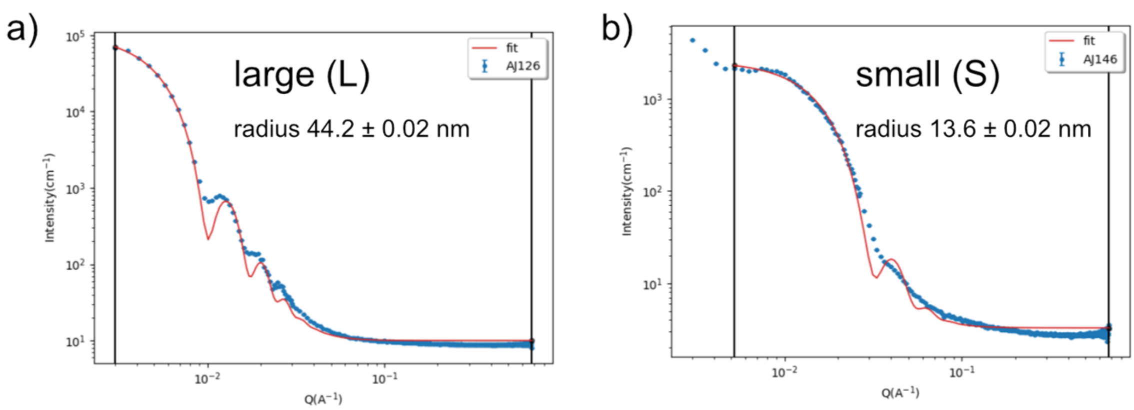

Figure S4. SAXS of polymeric nanoparticles in dispersion (1 wt%). The raw data (blue) is fit to a spherical model (red) using the software SASview.

3. Hybrid materials

Table S2. List of all hybrid materials fabricated in this study.

Sample name	Nanoparticle additive *np* (wt %)	Total buffer (mM)	Residual CNF charge after interaction with nanoparticles (µmol/g)	Molar ratio COOH:NH
CNF^0	0	0	-450	1:0
L_{10}^{low}	10	0.4	-358	1:0.12
L_{25}^{low}	25	1.1	-220	1:0.35
S_{10}^{low}	10	0.4	-358	1:0.23
S_{25}^{low}	25	1.1	-220	1:0.70
$L_{0.5}^{high}$	0.5	0.4	-445	1:0.01
L_{1}^{high}	1	0.9	-441	1:0.01
L_{5}^{high}	5	4.4	-404	1:0.05
L_{10}^{high}	10	8.8	-358	1:0.12
L_{25}^{high}	25	21.9	-220	1:0.35
$S_{0.5}^{high}$	0.5	0.4	-443	1:0.01
S_{1}^{high}	1	0.9	-436	1:0.02
S_{5}^{high}	5	4.4	-380	1:0.11
S_{10}^{high}	10	8.8	-310	1:0.23
S_{25}^{high}	25	21.9	-100	1:0.70
CNF^{high}	0	21.9	-450	1:0
CNF^{low}	0	1.1	-450	1:0

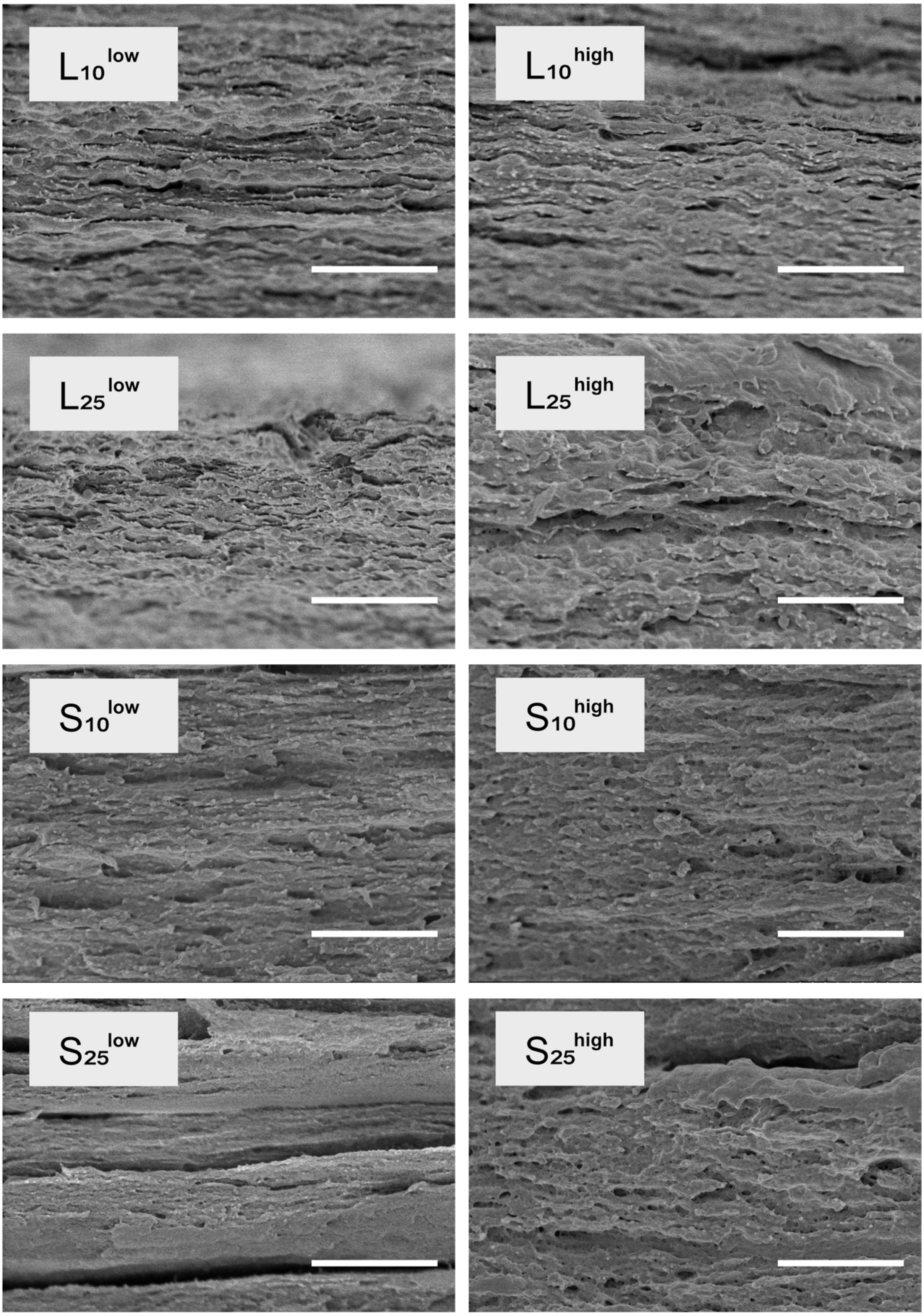

Figure S5. Comparison between high and low buffered materials in cryo-fractured surfaces. No consistent differences can be seen between low and high buffered samples in these cross-section images. Scale bar 1 µm.

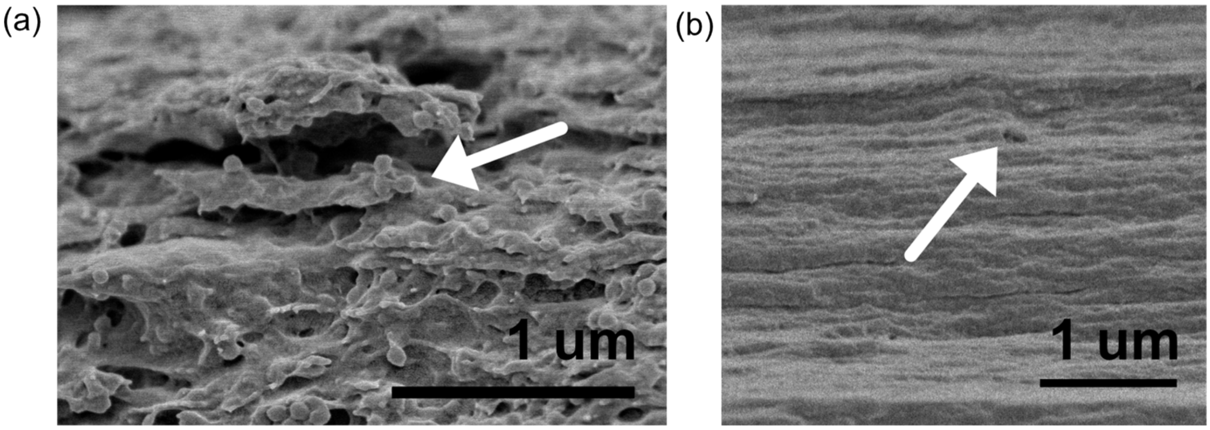

Figure S6. (a) Cryo-fractured cross-section imaged by FE-SEM of L_{25}^{high} showing that nanoparticles (white arrow) retain their spherical shape after hybridization into cellulose nanopapers. (b) Cryo-fractured cross-section of CNF^0 showing a potential nanopore.

Table S3. Ranges for cuts from radial and azimuthal integrations

Azimuthal integrations (around χ)				Radial integrations (q)		
		q value (Å)	d spacing (nm)			Angle (deg)
US100	start	0.006	104.7	USAXS radial x	start	260
	end	0.008	78.5		end	280
US20	start	0.027	23.3	USAXS radial y	start	170
	end	0.029	21.7		end	190
US10	start	0.05	12.6	WAXS radial x	start	260
	end	0.052	12.1		end	280
W200	start	1.04	0.60	WAXS radial y	start	170
	end	1.09	0.58		end	190

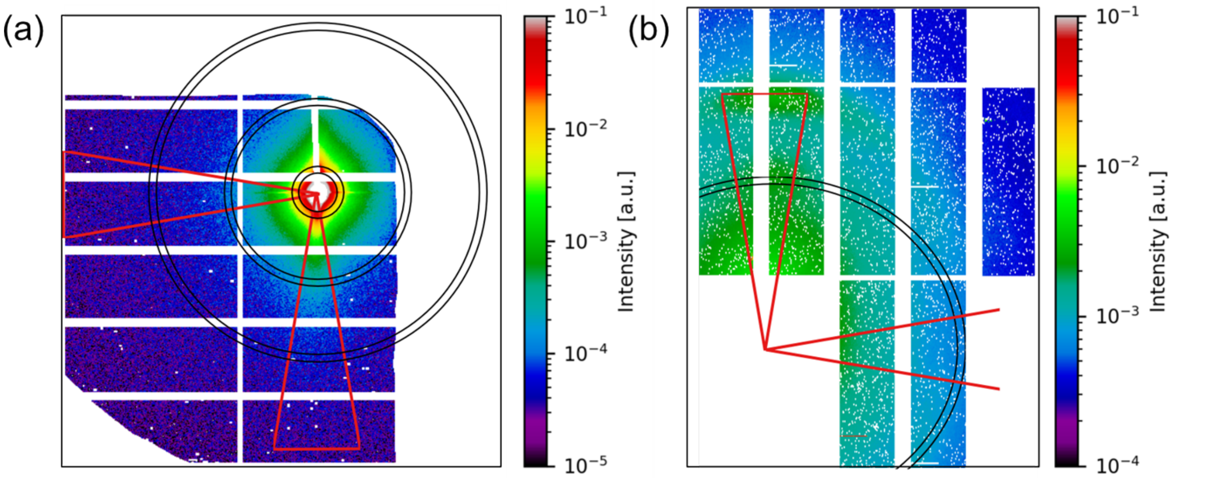

Figure S7. Representative USAXS (a) and WAXS (b) patterns to indicate cuts, these images from CNF^0. (a) USAXS pattern indicating 2 radial cuts (red) and 3 azimuthal cuts (black). (b) WAXS pattern indicating 2 radial cuts (red) and 1 azimuthal cut (black) at the [200] scattering plane.

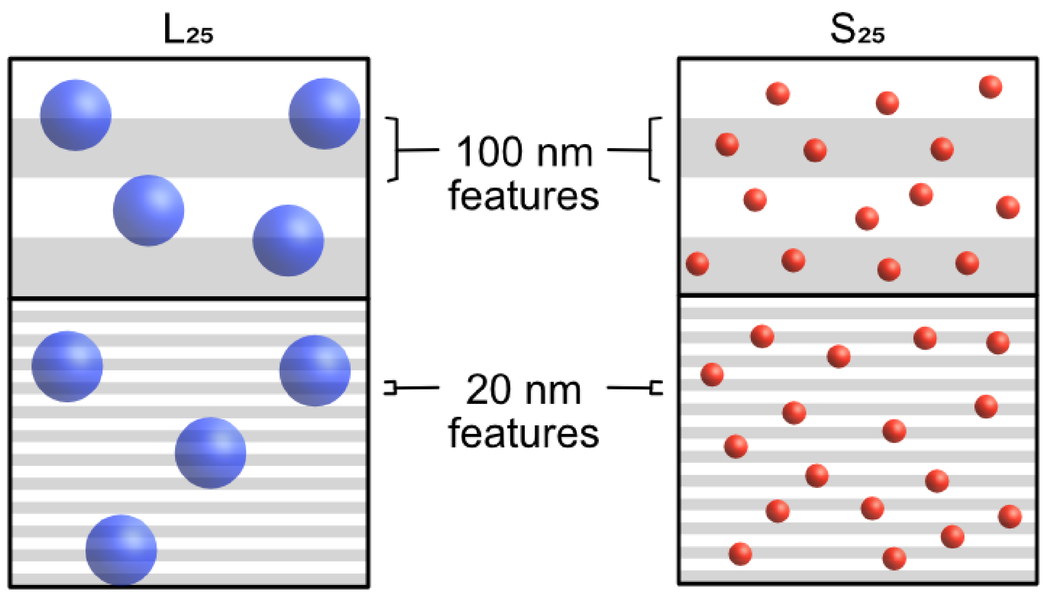

Figure S8. Schematic showing large and small particles fitting into cellulosic features of different sizes. For example large particles disrupt structures on all size ranges probed, but small particles seem to fit inside the self-assembled cellulose structures found at around 100 nm.

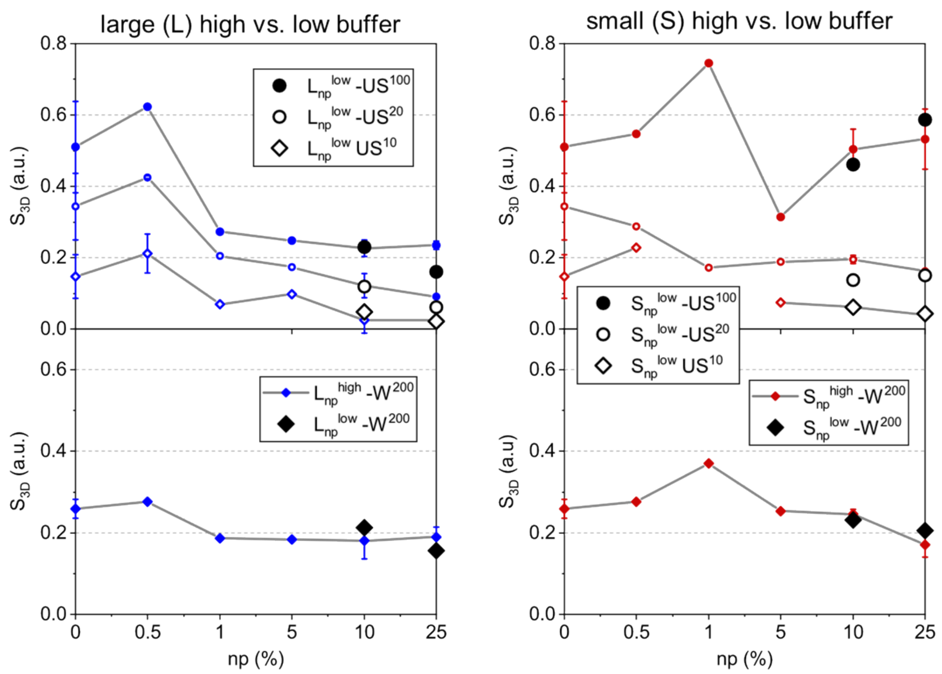

Figure S9. Alignment parameters for low buffered materials. No significant differences seen between high and low buffer samples in S_{3D}.

Table S4. Physical properties of hybrid nanopapers measured at 50 % relative humidity, 23 ^{o}C.

	Thickness		Density	
	um		g cm^{-3}	
	mean	sd	mean	sd
CNF^{0}	49	0.5	1.39	0.02
$L_{0.5}^{high}$	49	0.6	1.45	0.03
L_{1}^{high}	53	0.7	1.42	0.01
L_{5}^{high}	56	0.9	1.42	0.01
L_{10}^{high}	54	1.0	1.34	0.01
L_{25}^{high}	55	0.6	1.28	0.03
$S_{0.5}^{high}$	48	0.9	1.52	0.02
S_{1}^{high}	52	0.7	1.39	0.01
S_{5}^{high}	57	1.1	1.40	0.01
S_{10}^{high}	56	1.3	1.47	0.01
S_{25}^{high}	67	0.6	1.43	0.01

Table S5. Tensile properties of hybrid nanopapers (50 % relative humidity, 23 ^{o}C).

	E modulus		P modulus		Strain max		Stress max		Work of fracture		Tensile index	
	GPa		GPa		%		MPa		J m^{-3}		Nm g^{-1}	
	mean	sd	mean	sd	mean	sd	mean	sd	mean	sd	mean	sd
CNF^{0}	16.2	0.6	1.9	0.05	9.5	1.43	208	14	1325	245	150	10
$L_{0.5}^{high}$	15.1	1.3	2.0	0.08	6.5	2.78	170	34	782	455	121	21
L_{1}^{high}	15.5	0.3	1.6	0.05	8.2	3.14	182	39	1068	524	120	30
L_{5}^{high}	14.4	0.3	1.4	0.11	8.8	2.65	169	27	1033	395	110	11
L_{10}^{high}	14.4	0.3	1.3	0.11	7.6	2.05	155	16	847	296	113	21
L_{25}^{high}	11.9	0.3	0.9	0.05	7.6	3.11	127	19	730	367	87	12
$S_{0.5}^{high}$	14.4	0.3	2.0	0.17	6.5	2.32	175	30	804	395	112	23
S_{1}^{high}	14.1	1.5	1.8	0.08	7.4	3.58	171	42	910	559	131	28
S_{5}^{high}	13.8	0.3	1.2	0.18	8.0	1.82	155	15	894	246	121	19
S_{10}^{high}	12.1	0.8	0.9	0.07	10.6	3.81	152	29	1184	540	105	11
S_{25}^{high}	8.9	1.6	0.7	0.37	11.3	3.01	112	15	902	272	89	13

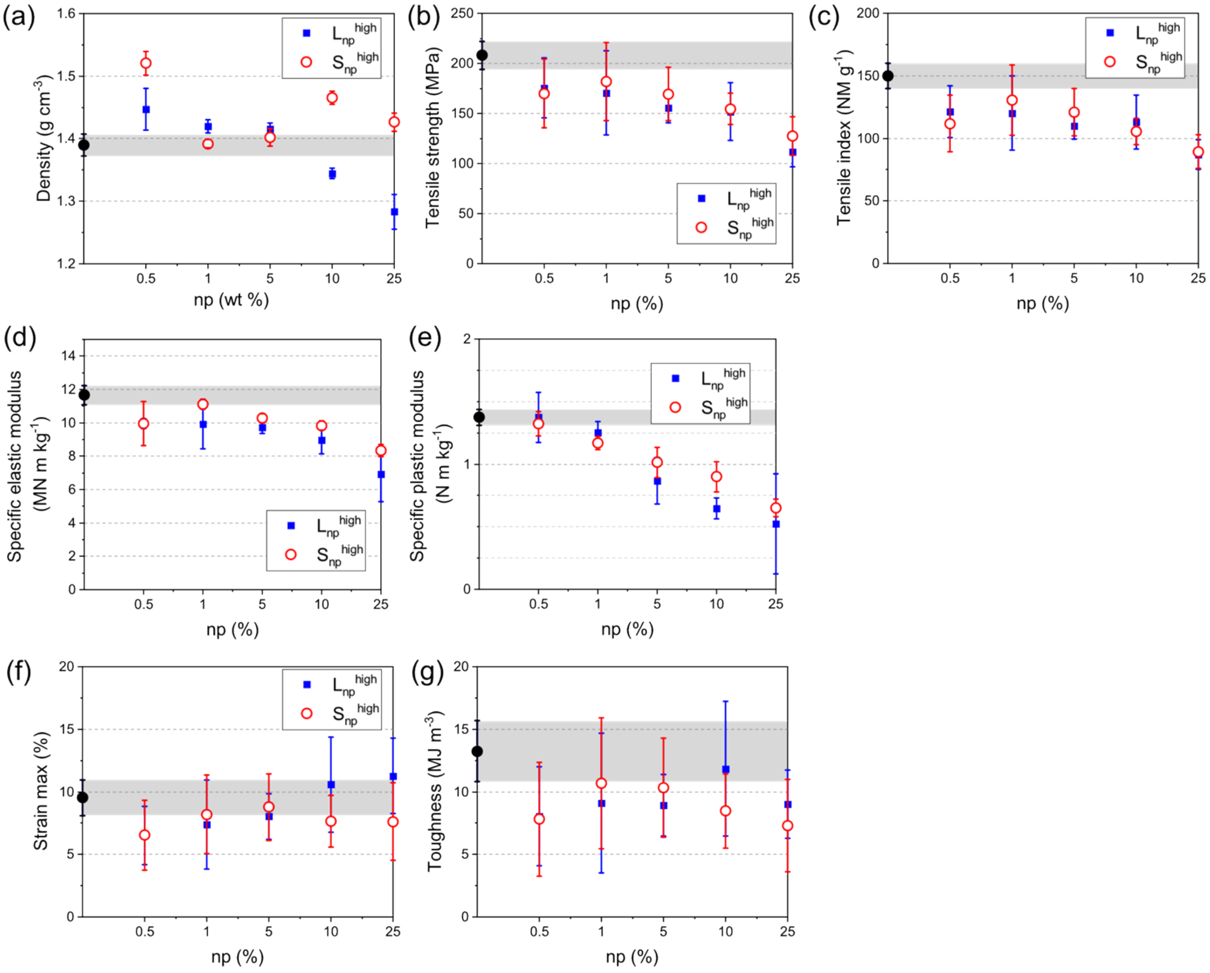

Figure S10. Tensile properties of hybrid nanopapers.

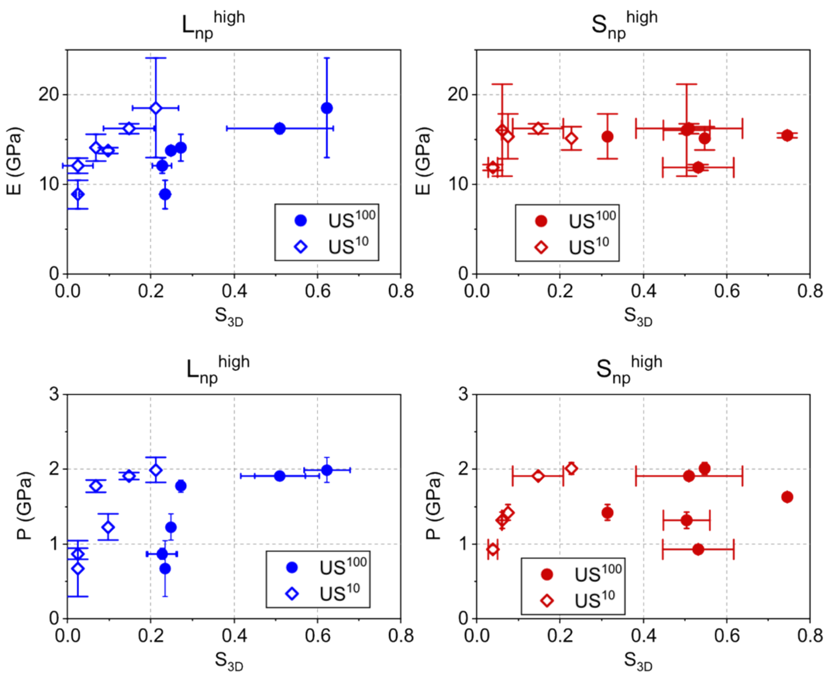

Figure S11. Correlations between alignment on different length scales, with elastic and plastic moduli.

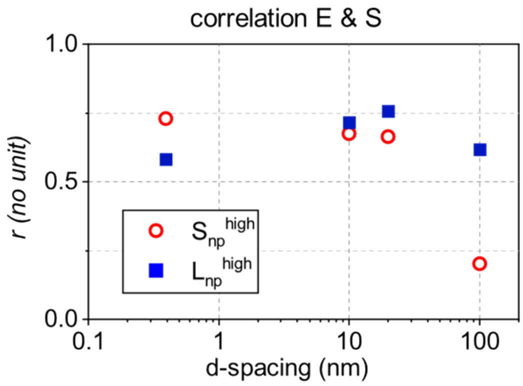

Figure S12. Pearson's correlation coefficients calculated between orientation parameters (S) and elastic modulus (E) at different length scales.